# Metallic Nanoshells with Semiconductor Cores: Optical Characteristics Modified by Core Medium Properties

**Rizia Bardhan,[†,⊥] Nathaniel K. Grady,[‡,⊥] Tamer Ali,[‡] and Naomi J. Halas[†,‡,§,*]**

[†]Department of Chemistry, [‡]Department of Electrical and Computer Engineering, and [§]Department of Physics and Astronomy and Laboratory for Nanophotonics, Rice University, Houston, Texas 77005, United States. [⊥]These authors contributed equally to this work.

**ABSTRACT** It is well-known that the geometry of a nanoshell controls the resonance frequencies of its plasmon modes; however, the properties of the core material also strongly influence its optical properties. Here we report the synthesis of Au nanoshells with semiconductor cores of cuprous oxide and examine their optical characteristics. This material system allows us to systematically examine the role of core material on nanoshell optical properties, comparing $Cu_2O$ core nanoshells ($\varepsilon_c \sim 7$) to lower core dielectric constant $SiO_2$ core nanoshells ($\varepsilon_c = 2$) and higher dielectric constant mixed valency iron oxide nanoshells ($\varepsilon_c = 12$). Increasing the core dielectric constant increases nanoparticle absorption efficiency, reduces plasmon line width, and modifies plasmon energies. Modifying the core medium provides an additional means of tailoring both the near- and far-field optical properties in this unique nanoparticle system.

**KEYWORDS:** cuprous oxide · gold nanoshell · plasmon-exciton · metal-semiconductor · high permittivity core · plasmon resonance

Nanoshells, nanoparticles with dielectric cores and metallic shells, have elicited increasing scientific and technological interest due to their ability to manipulate light in unique ways. Their optical properties are governed primarily by surface plasmons supported by the structure, whose resonance frequencies can be tuned by varying nanoparticle geometry.[1−4] Nanoshell surface plasmons give rise to strong local electromagnetic fields at the nanoparticle surface at resonance, which have been harnessed for a large number of photonic,[5−8] spectroscopic,[9−12] and biomedical[13−17] applications. The low-energy, symmetric, "bright" plasmon resonance of the nanoshell exhibits large far-field scattering and absorption cross-sections. Nanoshell plasmon mode properties can be modified by the presence of a surrounding or adjacent material, in a manner determined by the properties of the material in addition to its geometry.[4,18−21] Nanoshells can also modify the properties of an adjacent or surrounding material, creating new resonant modes through coupling or by modifying that material's excited-state lifetime and quantum yield.[22−25] Here we look at how a polarizable semiconductor medium within the central core of a nanoshell modifies its plasmonic properties.

The plasmon resonance frequencies of a nanoshell are a function of its internal dimensions and also of the dielectric permittivities of its core ($\varepsilon_c$), shell layer, and embedding medium ($\varepsilon_m$).[26,27] Core, shell, and embedding medium permittivities can also dramatically modify its absorption and scattering efficiencies. For simpler nanoparticles, like nanospheres or nanorods, the amount of light absorbed or scattered by the nanoparticle is a function of nanoparticle size. While smaller nanoparticles are predominantly absorptive, the absorption to scattering ratio decreases with increasing nanoparticle size, where larger particles are ultimately better light scatterers than light absorbers. In a concentric multilayer geometry, however, this relationship can be more complex. Recently we showed that the absorption and scattering efficiencies of gold−silica−gold layered nanoparticles can be modified, for fixed nanostructure size, by tailoring the thickness of the intermediate dielectric layer of the nanoparticle.[28] In this current work, we examine systematically how changing the core material in a nanoshell modifies its near- and far-field properties. Specifically, by changing the core material to a higher permittivity semiconductor, cuprous oxide ($Cu_2O$), the hybridized plasmons, the local field in and around the nanoparticle, and its absorption and scattering cross-sections are all significantly altered. $Cu_2O$/Au nanoshells ($\varepsilon_c \approx 7$) provide an important intermediate system between $SiO_2$/Au nanoshells ($\varepsilon_c = 2$)[26,29,30]

*Address correspondence to halas@rice.edu.

Received for review August 14, 2010 and accepted September 15, 2010.

**Published online September 22, 2010.**
**10.1021/nn102035q**

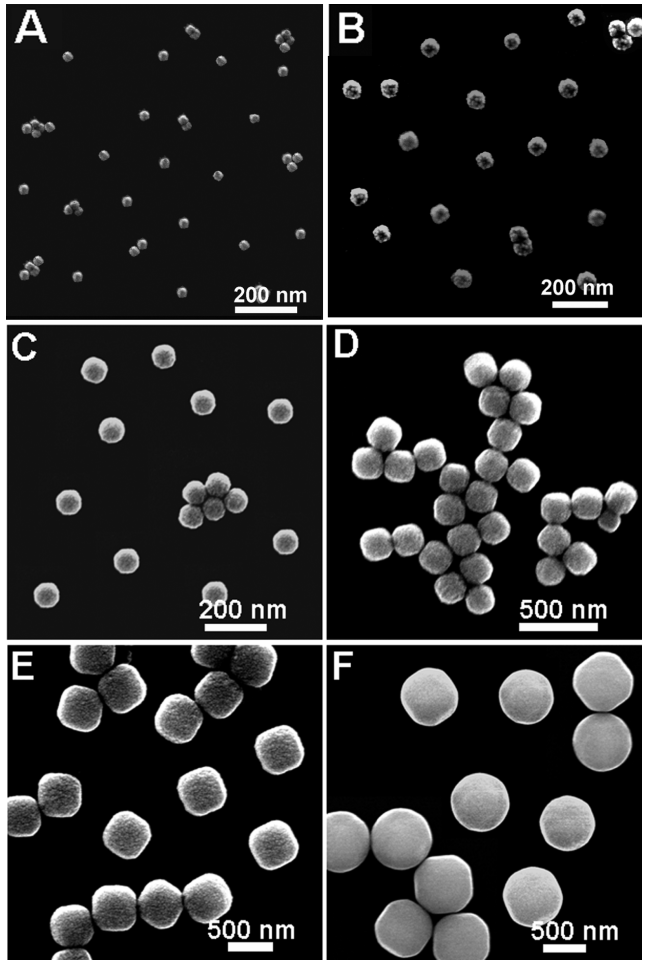


**Figure 1. SEM images of $Cu_2O$ nanoparticles. The radii of the nanoparticles are (A) 15 ± 0.5, (B) 30 ± 1, (C) 50 ± 2, (D) 100 ± 5, (E) 250 ± 30, and (F) 350 ± 50 nm.**

and mixed valency iron oxide nanoshells ($\varepsilon_c = 12$),[31] allowing us to examine how near- and far-field optical properties change as a function of core dielectric constant. The observed changes are analyzed using plasmon hybridization and Mie scattering theory. The unique ability to manipulate the optical properties of this nanoparticle by varying either internal geometry or material makes nanoshells extremely attractive for a wide variety of applications.

$Cu_2O$ is a semiconductor with a bandgap of 2.17 eV. Currently, it is primarily a material of interest for the study of exciton physics. In bulk $Cu_2O$, the lowest-energy "yellow" exciton is a prototypical example of a Wannier exciton, with energy levels following a simple hydrogenic model for $n \geq 2$[32,33] and oscillator strengths for $n \geq 3$.[34] The 1s state is distinct because its excitonic Bohr radius (0.53 nm) is comparable to the lattice constant (0.43 nm), resulting in several interesting properties. Electron−hole exchange interactions split the 1s exciton into a triply degenerate orthoexciton with total orbital angular momentum $J = 1$ and a paraexciton 12 meV below the orthoexciton with a total orbital angular momentum $J = 0$.[33−36] Due to the inversion symmetry of $Cu_2O$, direct creation of 1s excitons by one-photon optical transitions is only quadrupole allowed for orthoexcitons and completely forbidden for paraexcitons, but two-photon absorption may provide a route to populating these states. The small Bohr radius also results in a large binding energy, approximately 150 meV for the paraexciton and 140 meV for the orthoexciton. Because these excitons are strongly bound, they provide a promising system for the study of excitonic Bose−Einstein condensation (BEC).[34,37] In addition to BEC, these excitons have also been studied for other physical properties. The nearly ideal excitonic structure allows detailed studies of the manipulation of excitonic properties with magnetic, electrical, and optical fields. This has led to studies of the optically forbidden exciton states,[38−40] including the observation of dynamical Stark shifts in the exciton spectrum.[41] $Cu_2O$ is also a promising material for nonlinear optics.[42] By encapsulating $Cu_2O$ in a nanoscale Au shell, the nanoshell plasmons generated at the $Cu_2O$/Au interface could be used to control the coupling of $Cu_2O$ excitons to light. Coupling between plasmons and excitons can lead to the formation of hybrid plasmon-exciton, or plexciton, states.[23]

In this study, we experimentally fabricate nanoshells consisting of a $Cu_2O$ core coated with a thin Au shell ($Cu_2O$/Au) and, in conjunction with theoretical models, investigate the plasmonic properties of this composite nanoparticle.

## RESULTS AND DISCUSSION

The $Cu_2O$/Au nanoshells were fabricated in a stepwise manner by first synthesizing $Cu_2O$ nanoparticles in the size range of radius 15 ± 0.5 to 350 ± 150 nm in $H_2O$ at ambient temperature. The synthesis technique developed here was adapted and modified from one reported previously.[43] The nanoparticles were fabricated by reducing copper(II) salts with ascorbic acid in the presence of sodium hydroxide and poly (ethylene) glycol dithiol (HS-PEG-SH). Representative scanning electron microscope (SEM) images of the $Cu_2O$ nanoparticles verify their morphology and dimensions (Figure 1). X-ray powder diffraction (XRD) spectra confirming the composition of the $Cu_2O$ nanoparticles are shown in the Supporting Information (Figure S1). XRD spectra reveal the crystal structure and the lattice parameters verifying the formation of $Cu_2O$ nanoparticles by this synthesis technique. By varying the concentration of HS-PEG-SH, while keeping the concentration of the other reagents constant, the size of the $Cu_2O$ nanoparticles could be varied. PEG-dithiol acts as both a stabilizing agent as well as a shape-directing agent. By controlling the amount of PEG dithiol, the size can be manipulated as well as the shape can be altered from near-spherical to truncated cubic. The polydispersity was as low as ~3% for the nanoparticle radii <100 nm; however, for larger nanoparticles polydispersity increased beyond 10%.

This observation may indicate that at higher HS-PEG-SH concentrations, more nucleation sites are initiated, leading to faster growth kinetics and resulting in a larger size distribution. As the size of the nanoparticle increased, particularly for radii >100 nm, more particles exhibited truncated cubic rather than near-spherical shapes (Figure 1).[44,45] In addition, the HS-PEG-SH molecules also terminate the $Cu_2O$ nanoparticles with thiol groups, which can attach to Au without the need for further functionalization to nucleate subsequent Au layer growth.

The $Cu_2O$ nanoparticles by themselves display a size-dependent optical response (Figure 2). Optical images (Figure 2A) of the $Cu_2O$ nanoparticles dispersed in $H_2O$ show that solutions of $Cu_2O$ nanoparticles change color from bright yellow to orange with increasing nanoparticle size, consistent with previous reports.[43] Experimental extinction spectra of $Cu_2O$ nanoparticles of different size, dispersed in $H_2O$, show size-dependent spectral features (Figure 2B). In this figure, the nanoparticle radius is indicated to the right of each optical spectrum. The extinction spectra of the smaller nanoparticles (radii ≤50 nm) exhibit strong Rayleigh scattering and a small peak at 440 nm. As the nanoparticle size is increased to a 100 nm radius, new spectral features are observed in the visible region of the spectrum near 530 nm and in the near-infrared range near 700 nm. With increasing nanoparticle size, these spectral features redshift, and additional features in the near and mid-infrared can be observed. These additional extinction peaks are due to scattering at the Mie resonances of the particles.[47,48] Theoretical extinction spectra of the $Cu_2O$ nanoparticles (Figure 2C) were obtained using Mie theory, assuming a spherical geometry with diameters matching the experimentally obtained nanoparticle sizes and the complex frequency-dependent empirical dielectric function tabulated in Palik[46,49] for bulk $Cu_2O$. The calculated extinction spectra correspond well to the measured spectra for all nanoparticle sizes studied. The small disparities observed between the calculated and experimental spectra, specifically in the case of the larger nanoparticles, are likely due to a combination of polydispersity, variations in nanoparticle geometry, and small variations in the dielectric function of the fabricated nanoparticles from the values for bulk $Cu_2O$ obtained from the literature.[45,46,49]

The freshly prepared $Cu_2O$ nanoparticles show some degree of cross-linking due to the presence of the SH-PEG-SH on their surface. This cross-linking between adjacent $Cu_2O$ nanoparticle results in formation of self-assembled ordered arrays when a droplet of the nanoparticle solution is allowed to dry in ambient at room temperature on a silicon or quartz substrate. SEM images of the arrays are provided in the Supporting Information (Figure S2).

$Cu_2O$/Au nanoshells are fabricated by seed-mediated electroless plating of Au onto the thiol-terminated $Cu_2O$ nanoparticles.[29,30] The freshly prepared $Cu_2O$ nanoparticles were immediately used for preparation of nanoshell precursor particles to avoid excessive cross-linking between $Cu_2O$ nanoparticles. Small Au nanoparticles (~2 nm in diameter) are immobilized onto the surface of the $Cu_2O$ cores. The immobilized Au nanoparticles act as nucleation sites for electroless plating of Au onto the surface of the core nanoparticles, resulting in the gradual formation of a continuous and complete metal shell layer upon reduction. Further metal deposition onto the nanoparticle increases the

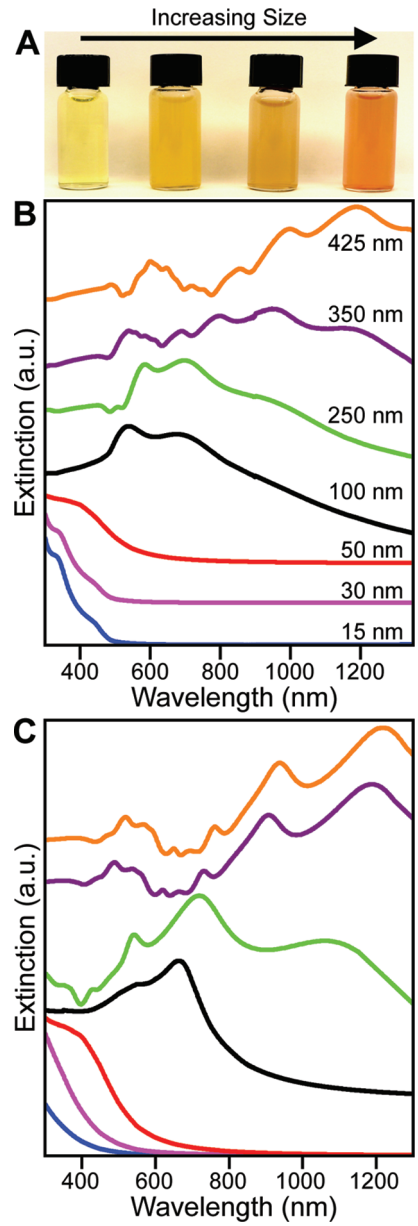


**Figure 2. (A) Optical image of $Cu_2O$ nanoparticles of various sizes suspended in aqueous solution. (B) Experimental absorption spectra of the $Cu_2O$ nanoparticle suspensions shown in (A). Nanoparticle radius corresponding to the spectrum is indicated on right. Spectra are offset for clarity. (C) Absorption spectra of $Cu_2O$ nanoparticles in aqueous media ($n$ = 1.33) calculated using Mie theory with an empirical $Cu_2O$[46] dielectric function. The spectra are color coordinated with part (B) and offset for clarity.**

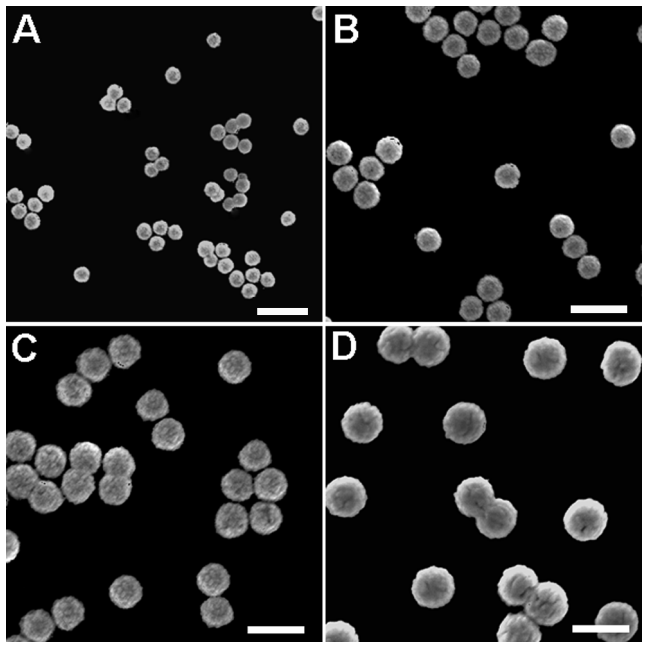


**Figure 3. SEM images of $Cu_2O$/Au-NS of different sizes. (A) [$r_1$, $r_2$] = [15, 32] nm, (B) [$r_1$, $r_2$] = [30, 46] nm, (C) [$r_1$, $r_2$] = [40, 54] nm, and (D) [$r_1$, $r_2$] = [50, 65] nm. The scale bar is 200 nm.**

Au layer thickness. SEM images of $Cu_2O$/Au nanoshells fabricated on cores ranging in size from a radius of 15−50 nm are shown in Figure 3. (The standard parametrization of nanoshell geometries is used here, with $r_1$ = core radius and $r_2$ = total nanoparticle radius.) While $Cu_2O$ nanoparticles can be synthesized in different shapes,[43,50] the growth of a uniform Au layer on the nanoparticles modifies the overall shape of the nanoparticle, resulting in a spherical morphology of the completed nanoshell. This synthesis route allows the fabrication of uniform, monodisperse, stable suspensions of core−shell nanoparticles in the sub-150 and -100 nm size regimes. Additional SEM images of $Cu_2O$/Au precursor particles used for nanoshell synthesis and TEM micrographs of $Cu_2O$/Au nanoshells are provided in the Supporting Information (Figure S3). The Au coating also enables suspension of the nanoparticles in $H_2O$ and provides a biocompatible surface that can be straightforwardly functionalized with a wide range of molecules by well-established protocols.

The optical properties of $Cu_2O$/Au nanoshells clearly demonstrate the effect of nanoshell aspect ratio $r_1/r_2$ on the spectral response of the nanoparticle in solution (Figure 4). The optical images of $Cu_2O$/Au nanoshells in aqueous solution (Figure 4A) indicate a change in solution color from purple to blue as the size and aspect ratio of the $Cu_2O$/Au nanoshells is increased. The observed extinction spectra of the $Cu_2O$/Au nanoshells with differing aspect ratios corresponding to the SEM images (Figure 3) are shown in Figure 4B. The extinction spectra span the visible to the NIR region of the optical spectrum with the smallest size [$r_1$, $r_2$] = [15, 32] nm displaying a plasmon resonance at 610 nm.

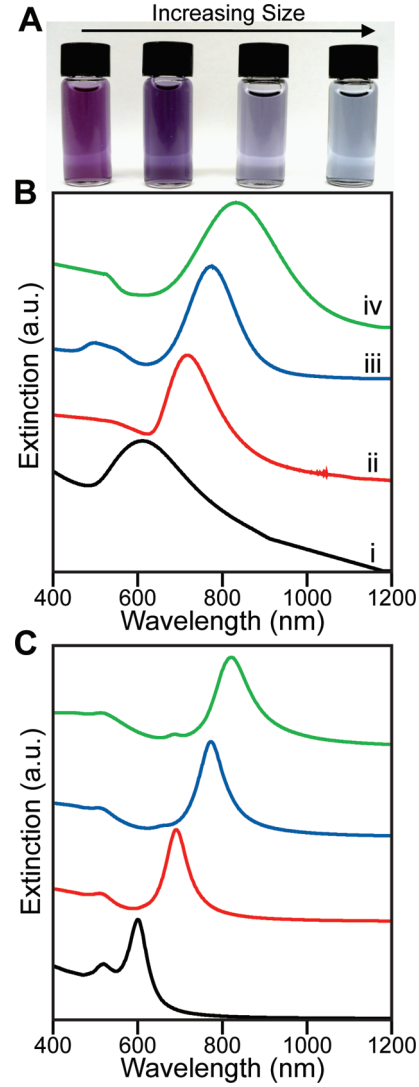


**Figure 4. (A) Optical image of $Cu_2O$/Au-NS of increasing core size and constant shell thickness dispersed in $H_2O$. (B) Experimental extinction spectra of $Cu_2O$/Au-NS of different sizes: (i) [$r_1$, $r_2$] = [15, 32], $\lambda_{max}$ = 610 nm; (ii) [$r_1$, $r_2$] = [30, 46], $\lambda_{max}$ = 705 nm; (iii) [$r_1$, $r_2$] = [40, 54], $\lambda_{max}$ = 780 nm; and (iv) [$r_1$, $r_2$] = [50, 65], $\lambda_{max}$ = 830 nm. Spectra are offset for clarity. (C) Extinction spectra of the $Cu_2O$/Au-NS in aqueous medium calculated using Mie theory with empirical dielectric functions for the Au shell[51] and $Cu_2O$[46] core. The spectra are colored to correspond with the spectra in (B) and offset for clarity.**

With increasing nanoshell size the plasmon resonance redshifts to 705, 780, and 830 nm, respectively (Figure 4A). In the quasistatic limit, where the size of the nanoshell is much smaller than the spatial wavelength of light, the plasmon resonance energies are expected to be determined by aspect ratio $r_1/r_2$.[18] As the aspect ratio is increased, the plasmon resonance shifts to longer wavelengths.[26,52] In Figure 4, the shell thickness is held nearly constant, while the core size is increased, increasing the aspect ratio from 0.47 to 0.77, resulting in a concomitant redshift of the plasmon resonance. The corresponding theoretical extinction spectra of the $Cu_2O$/Au nanoshells (Figure 4C) were obtained using

Mie theory, assuming a spherical core and shell geometry, where the $Cu_2O$ core was modeled using the same frequency-dependent dielectric function as in Figure 2C,[46,49] the shell was modeled using the empirical dielectric function measured by Johnson and Christy (JC Au),[51] and the $H_2O$ medium was modeled using a constant dielectric $\varepsilon_m = 1.77$. The theoretical spectra and peak positions correspond well with the experimental extinction spectra, suggesting that $Cu_2O$ nanoparticles $\leq$100 nm are mostly spherical and that the small fraction of truncated cubic shapes present does not affect the ensemble plasmon line shape or peak position. For the smallest fabricated $Cu_2O$/Au nanoshells with $[r_1, r_2] = [15, 32]$ nm, the observed plasmon line width is larger than theoretical predictions, probably due to inhomogeneities in the thickness of the Au shell layer.[3,53] Theoretical spectra of $Cu_2O$/Au nanoshells with truncated cubic cores are provided in the Supporting Information, Figure S4. The calculated spectra clearly suggest that in the case of truncated cubic cores, the plasmon peaks shift to longer wavelengths. Additionally, the antiboding plasmon peak is significantly stronger than in the case of spherical cores. This concept has been discussed previously[31] and is beyond the scope of this paper.

The plasmon resonance tunability in this system was also studied by varying the Au shell thickness for a fixed core size. Experimental extinction spectra of $Cu_2O$/Au nanoshells with the same core radius 40 $\pm$ 2 nm and varying shell thicknesses, for a total outer radius of 54 $\pm$ 5, 57 $\pm$ 5, 60 $\pm$ 7, and 63 $\pm$ 11 nm, are shown in Figure 5A. Theoretically obtained spectra calculated using Mie theory and the same parameters used in the calculations shown in Figure 4 correspond well to the experimental extinction spectra (Figure 5B). With a core of constant radius and increasing Au shell thickness the aspect ratio $r_1/r_2$ decreases, from 0.74 to 0.63 in this sequence, and the plasmon resonance blueshifts to shorter wavelengths, from 780 to 710 nm.

These trends can be understood within the plasmon hybridization picture, a theoretical approach useful for understanding the resonant modes of complex metal nanoparticles and nanostructures.[27,54,55] Unlike Mie theory, where the electromagnetic boundary value problem is solved with the materials only entering as an arbitrary dielectric function, plasmon hybridization directly considers the conduction electrons in the metal responsible for the plasmon resonances. The conduction electrons are modeled as an incompressible, irrotational fluid on a fixed positive background due to the ion cores. Plasmons are then deformations of this electron fluid. For a complex structure, the plasmon modes can be expressed as the interaction between the primitive plasmon modes associated with each metal surface. In the case of a nanoshell, plasmon modes supported by a solid sphere ($\omega_s$) and a hollow spherical cavity ($\omega_c$) interact to form hybrid bonding and antibonding nanoshell plasmon modes in a manner analogous to wave function hybridization in molecular orbital theory (Figure 6). The interaction between the sphere and cavity plasmons is a function of the aspect ratio $x = r_1/r_2$. As the aspect ratio is increased, the low-energy bonding dipole mode ($\omega_+$) shifts to lower energy while the high-energy antibonding dipole ($\omega_-$) shifts to higher energy (Figure 6i). This is exactly the behavior observed experimentally for the bonding dipole resonance (Figures 4 and 5). In the limit $x \rightarrow 0$ (*i.e.*, vanishing core radius), the interaction between the cavity and sphere plasmons vanishes, and the nanoshell plasmon resonances asymptotically approach the isolated sphere and the cavity plasmon resonances (Figure 6i). The plasmon hybridization model describes the metal response in an equivalent way to the standard Drude model. In order to compare Mie theory with plasmon hybridization, a Drude model dielectric function $\varepsilon(\omega) = \varepsilon_\infty - \omega_p^2/(\omega^2 + i\Gamma\omega)$, where $\varepsilon_\infty = 8$ is the background dielectric due to the ion cores, $\omega_p = 9.06$ eV is the bulk plasmon frequency, and $\Gamma = 0.1$ eV is the damping rate (Figure 6iii) is used.

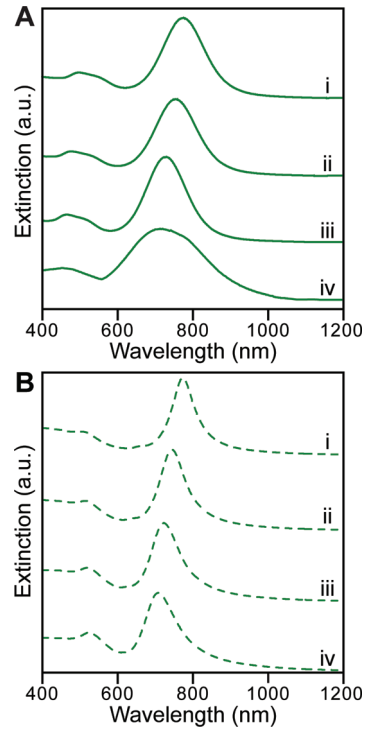


**Figure 5. (A) Experimental extinction spectra of $Cu_2O$/Au nanoshells for core radius $r_1 = 40 \pm 2$ nm with varying Au shell thickness ($r_2$-$r_1$): (i) $r_2 = 54 \pm 5$, (ii) $r_2 = 57 \pm 5$, (iii) $r_2 = 60 \pm 7$, and (iv) $r_2 = 63 \pm 11$ nm. (B) Extinction spectra of $Cu_2O$/Au nanoshells of similar sizes as the experimentally synthesized nanoparticles calculated using Mie theory with empirical dielectric functions for the Au shell[51] and $Cu_2O$[46] core.**

The resonance energies of the primitive plasmons depend on the adjacent dielectric material; increasing either the embedding medium ($\varepsilon_m$) or the core ($\varepsilon_c$) dielectric constants shifts the sphere or cavity plasmon, respectively, to longer wavelengths. The embedding

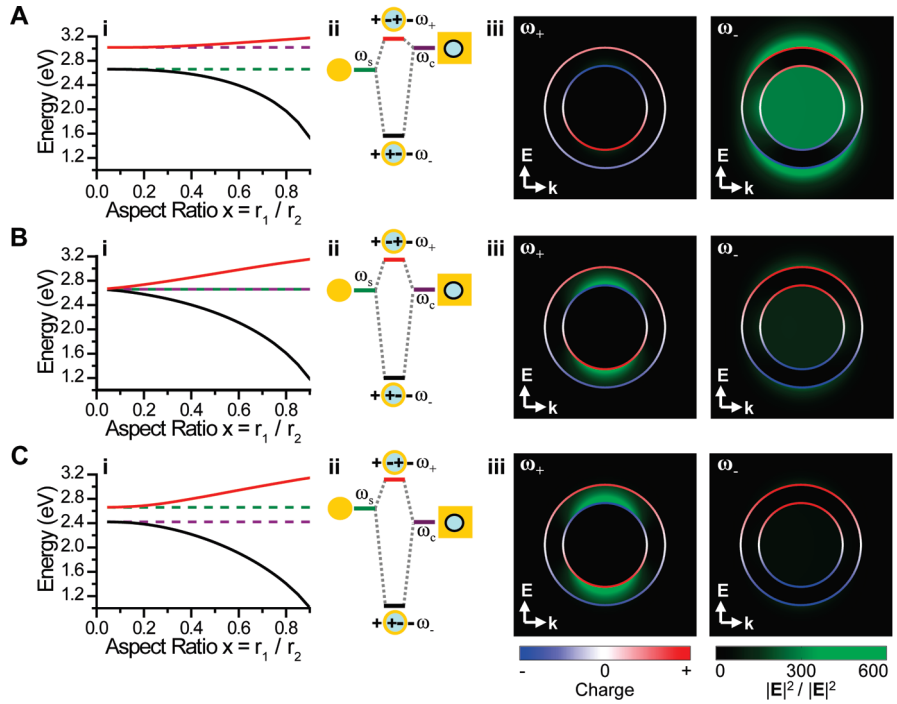


**Figure 6. Nanoshells with a core dielectric constant of (A) $\varepsilon_c = 2$ ($SiO_2$), (B) $\varepsilon_c = 7.2$ ($Cu_2O$), and (C) $\varepsilon_c = 12$ (mixed valency iron oxide) cores in a Drude shell layer calculated using plasmon hybridization theory. Structures are embedded in $H_2O$ ($\varepsilon_m = 1.8$). (i) Antibonding ($\omega_+$, red) and bonding ($\omega_-$, black) nanoshell dipole plasmon resonance energies calculated as a function of aspect ratio. The primitive cavity ($\omega_c$, purple) and sphere ($\omega_s$, green) plasmon resonances are indicated as horizontal dashed lines. (ii) Hybridization diagrams, each corresponding to the adjacent graph for the case of aspect ratio $x = 0.9$. (iii) Surface charge distributions and near-field intensity enhancements at the antibonding ($\omega_+$) and bonding ($\omega_-$) plasmon resonance energies of a quasistatic $[r_1, r_2] = [7, 10]$ nm nanoshell using Mie theory with a Drude shell layer.**

medium $\varepsilon_m$ is often determined by application, for example, when the nanoparticles are immersed in an aqueous environment ($\varepsilon_m \sim 1.8$), as is often the case in biological or sensing applications. In contrast, the choice of core material $\varepsilon_c$ has fewer constraints and provides an independent approach for changing the plasmon resonant properties of nanoshells beyond modifying geometry or embedding medium. For a nanoshell modeled using an empirical Au dielectric function, the sphere and cavity resonance energies are degenerate for $\varepsilon_c \sim 5.5$ when immersed in air ($\varepsilon_m = 1$) and $\varepsilon_c \sim 8$ when immersed in water ($\varepsilon_m = 1.8$). The sphere and cavity plasmon resonances shift slightly when a Drude approximation is used for Au. In this case, the sphere and cavity resonance energies are degenerate for $\varepsilon_c \sim 4$ when the nanoshell is in air or $\varepsilon_c \sim 7.2$ when the nanoshell is in water.

To examine the role of the core dielectric function, we compare $Cu_2O$ core nanoshells to nanoshells with core oxides possessing significantly lower and higher core dielectric constants: $SiO_2$ core nanoshells[26,29,30] and mixed valency iron oxide core nanoshells[31] (Figure 6). For the $SiO_2$ nanoshell (Figure 6A), the cavity plasmon resonance energy is significantly higher than the sphere plasmon. The interaction between the sphere and cavity plasmon is shown schematically in the plasmon hybridization diagram of Figure 6A (ii). This interaction results in a high-energy antibonding resonance composed of an antisymmetric combination of sphere and cavity primitive plasmons and a low-energy bonding plasmon composed of a symmetric combination of the sphere and cavity plasmons. The nature of the nanoshell modes can be seen by examining the evolution of the nanoshell plasmon modes as the coupling is turned on by increasing aspect ratio $x$ from near 0 to near 1 (Figure 6A (i)). In this case, the $\omega_+$ mode evolves primarily from the cavity plasmon and the $\omega_-$ primarily from the sphere plasmon. The dielectric constant of $Cu_2O$ increases in the near-IR from 6.8 to 8.4 with increasing energy (Supporting Information Figure S5), resulting in nearly degenerate cavity and sphere plasmon mode energies for the nanoparticle in aqueous solution (Figure 6B). The resulting $Cu_2O$/Au nanoshell plasmons are therefore composed of a nearly equal mixture of sphere and cavity plasmons. Mixed valency iron oxide core nanoshells, with an effective $\varepsilon_c \sim 12$, provide an example of the case where the cavity plasmon is at a much lower energy than the sphere plasmon (Figure 6C).[31] In this case, the $\omega_+$ mode now has a larger admixture of the sphere plasmon, and the $\omega_-$ mode has a larger admixture of the cavity plasmon. The symmetry of the modes is however unchanged with increasing values of the core dielectric: the $\omega_+$ mode is still the antisymmetric combination of the primitive plasmons, and the $\omega_-$ mode is the symmetric combination of the primitive plasmons.

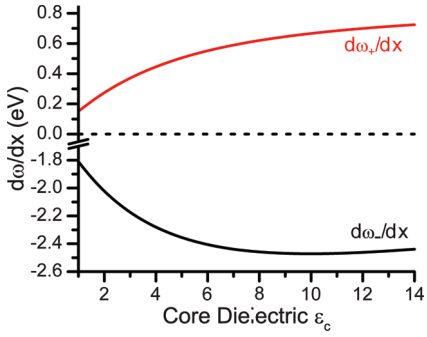


**Figure 7. Geometric tunability of the $\omega_+$ and $\omega_-$ dipole plasmon resonances of a nanoshell as a function of core dielectric function $\varepsilon_c$ calculated using plasmon hybridization with a Drude shell and $\varepsilon_m = 1.8$. The tunability is evaluated at an aspect ratio $x = r_1/r_2 = 0.7$.**

We calculated charge distribution and near-field intensity enhancement for each of the three core materials in our study to observe the structure of each plasmon mode. These calculations were performed using Mie theory for a nanoshell in the quasistatic limit ($[r_1, r_2] = [7, 10]$ nm) with the metal described by a Drude model dielectric function to match the plasmon hybridization calculations. As expected, the charges on the inner and outer surface of the Au shell are opposite in sign for the $\omega_+$ mode, composed of an antisymmetric combination of sphere and cavity primitive plasmons, and are the same sign for the symmetric $\omega_-$ mode. The local-fields are consequently strongest in the regions between opposite charges. For the $\omega_+$ mode, the local-field intensity is strongest inside the metal shell, while the $\omega_-$ mode produces a strong field on the outer surface of the metal shell and inside the core. Interband transitions in Au have been neglected here for clarity; in realistic structures the antibonding modes above ~2.5 eV would be damped significantly due to the Au interband transition. In the quasistatic limit, only the sphere plasmon couples to light. The coupling of the nanoshell plasmon modes to light is therefore determined by the relative contribution of the sphere plasmon to the nanoshell plasmon mode.[56]

From the tuning curves shown in Figure 6i, it is evident that the magnitude of the plasmon splitting between nanoshell plasmons varies with core dielectric function. To examine this further, the tunability of the $\omega_+$ and $\omega_-$ plasmons as a function of core dielectric constant is evaluated by taking the derivative of the plasmon energy with respect to aspect ratio, $d\omega_\pm/dx$ (Figure 7). While the tuning curves in Figure 6i are clearly not linear with respect to $x$, the overall trends with respect to core dielectric do not change when $d\omega_\pm/dx$ is evaluated around different values of $x$. The tunability of both the bonding and antibonding modes increases significantly when the core dielectric is increased (Figure 7).

Based on this understanding of the effect of core dielectric constant on nanoshell plasmon modes in the quasistatic limit, we examine the effect of core dielectric constant on the far-field spectral response of finite-size nanoshells. We calculate the far-field extinction, absorption, and scattering spectra of $SiO_2$/Au (solid), $Cu_2O$/Au (dashed), and mixed valency iron oxide (dotted) nanoshells for three different nanoparticle sizes: $[r_1, r_2] = [30, 42]$, $[40, 52]$, and $[60, 72]$ nm (Figure 8) in $H_2O$. In this series of calculations we use an empirical Au dielectric function;[51] therefore the antibonding plasmons are damped by the interband transition in Au, and the spectra obtained are dominated by bonding plasmon modes. The $SiO_2$ and mixed valency iron oxide cores are modeled using the same constant dielectric function as in the plasmon hybridization calculations, while a realistic frequency-dependent dielectric function[46,49] is used for $Cu_2O$. The spectral features all shift to longer wavelengths with increasing core dielectric function, as expected from our earlier plasmon hybridization analysis. It is clearly apparent that as the core dielectric is increased from that of $SiO_2$ to $Cu_2O$ and finally iron oxide, the overall scattering efficiency decreases dramatically, and the absorption increases significantly for nanoshells of the same dimensions, despite only a slight decrease in extinction. The line width is also reduced as the core dielectric constant increases. Understanding these observations requires a consideration of the role of finite size (beyond the quasistatic regime) in the nanoparticle optical response.

Phase retardation effects—the spatial variation of the phase of the incident field spanning the particle and the non-negligible propagation time of the optical wave across the particle—play a significant role in determining the optical response of nanoparticles such as those considered here. Increasing the core dielectric allows the bonding plasmon resonance to be tuned to longer wavelengths without changing the overall size of particle. In other words, increasing the core dielectric function decreases the optical path length across the nanoparticle, which reduces the effective size of the nanoparticle with respect to the wavelength of incident light. Consequently, retardation effects decrease in importance as the core dielectric is increased. Much like antennas in the RF, nanoparticles that are much smaller than the wavelength of light do not efficiently radiate electromagnetic energy. The decrease in the relative size of the nanoshell compared to the wavelength results in reduced scattering relative to absorption when the core dielectric is increased.[31,56] For the $[r_1, r_2] = [30, 42]$ nm nanoshell (Figure 8A) the scattering and absorption efficiencies for the $SiO_2$/Au nanoshell are almost the same, while for the $Cu_2O$/Au nanoshell the absorption is much stronger. Increasing the nanoshell size to $[r_1, r_2] = [40, 52]$ nm results in the

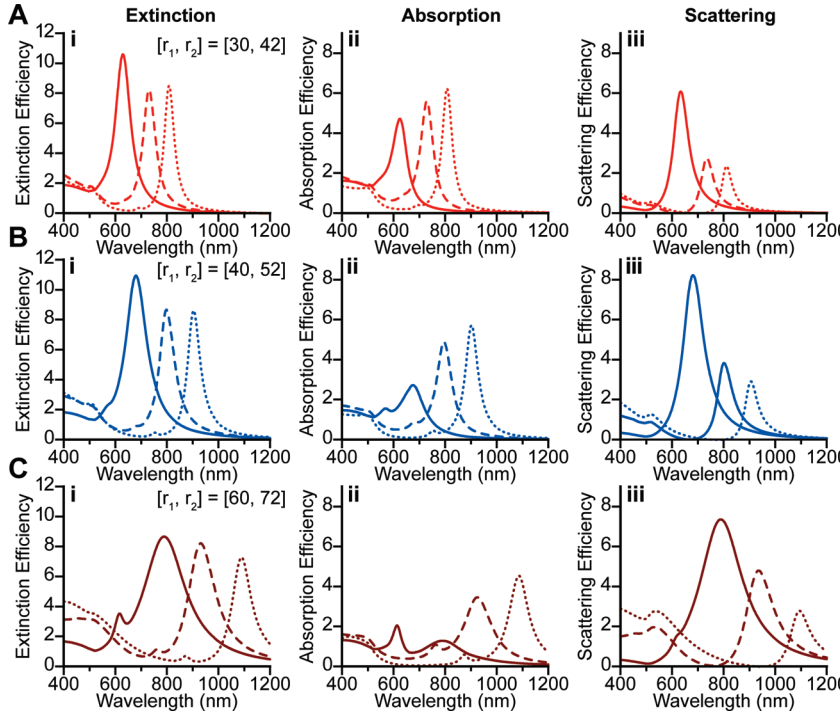


**Figure 8. Calculated (i) extinction, (ii) absorption, and (iii) scattering efficiency spectra of $SiO_2$/Au (solid line), $Cu_2O$/Au (dashed line), and iron oxide/Au (dotted line) nanoshells with the geometry (A) $[r_1, r_2] = [30, 42]$, (B) $[r_1, r_2] = [40, 52]$, or (C) $[r_1, r_2] = [60, 72]$ nm. These spectra were calculated using Mie theory using frequency-dependent empirical dielectric functions for the Au shell[51] and $Cu_2O$ core,[46] $\varepsilon_c = 2.04$ for the silica core and $\varepsilon_c = 12$ for the iron oxide core.**

$Cu_2O$/Au nanoshell almost equally absorbing and scattering light, while the $SiO_2$/Au nanoshell now predominantly scatters. The same trend continues for the $[r_1, r_2] = [60, 72]$ nm nanoshells. Interestingly, even for these larger nanoshells, the mixed valency iron oxide nanoshells are still strong absorbers. Quantitatively, the optical size of the particles can be expressed as the size parameter $ka$, where $k = 2\pi/\varepsilon_m^{1/2}\lambda$ is the wave vector of the incident light, and $a = r_2$ is the overall radius of the particle. The optical size of the $[r_1, r_2] = [30, 42]$ nm $SiO_2$ core nanoshell on its dipole resonance and the $[r_1, r_2] = [40, 52]$ nm $Cu_2O$ core nanoshell are both $ka = 0.23$. Nonetheless, the relative contribution of scattering to the extinction spectrum is still larger for the $SiO_2$ core nanoshell of the same optical size indicating that phase retardation is only part of the reason for the increased absorption.

This slower increase in relative scattering and absorption cross-sections with optical size for nanoshells with a $Cu_2O$ core compared to a $SiO_2$ core can be explained in terms of plasmon hybridization. Because the sphere and cavity primitive plasmon modes are closer in energy for nanoshells with a $Cu_2O$ core, the bonding dipole nanoshell mode has a larger admixture of the cavity plasmon than in the case of a lower dielectric constant core. In other words, with an increased core dielectric function the core medium is polarized more strongly, opposing the charge distribution on the inner surface of the nanoshell. In both pictures, this results in a mode with stronger energy confinement within the nanoparticle. The mode is therefore lossier and radiates less efficiently to the far field. This increasing loss with stronger confinement of the local fields is a common property in many plasmonic structures.[25,57] The decreased line width of $Cu_2O$/Au nanoshells relative to $SiO_2$ nanoshells is a direct consequence of this decreased contribution of scattering to the overall cross-section. Scattering is essentially the radiative decay of the plasmon. A reduction in scattering corresponds to a reduction in the rate of energy loss from the plasmon and, therefore, a narrower line width. A similar effect has previously been observed in multilayer Au−silica−Au nanoshell structures. In this case, changing the intermediate silica layer thickness allowed the resonance wavelength to be tuned without varying the overall particle size, resulting in a variation in the relative contribution of absorption and scattering to the overall extinction of the nanoparticle.[28]

The most significant difference in the material properties of $Cu_2O$ and $SiO_2$ is that $Cu_2O$ is a semiconductor with a bandgap in the visible region of the spectrum. Losses due to absorption in the semiconducting $Cu_2O$ core, absent in a transparent dielectric like $SiO_2$, may be expected to contribute to the increased absorption efficiency. Calculated extinction, scattering, and absorption efficiencies of $Cu_2O$/Au nanoshells using constant real permittivity of 7.6 for the cores demonstrate that the absorption

and scattering efficiencies at the bonding dipole resonance, which is the dominant peak in these spectra, are comparable for both the constant dielectric and the frequency-dependent dielectric function (see Supporting Information, Figures S6 and S7). Surprisingly, despite the small change in overall extinction, separating the absorption into the contribution from losses in the core and shell indicates that >25% of the energy is absorbed in the core at the bonding dipole resonance for the case of a complex (non-negligible imaginary part) frequency-dependent dielectric function, as in the case of $Cu_2O$. This is because, in the experimentally relevant size regime, the additional damping due to absorption by the $Cu_2O$ is small compared to the radiative damping. To the short wavelength side of the bonding dipole, the imaginary part of the core dielectric has a more significant effect. This is because the bonding quadrupole, visible as a shoulder on the short wavelength side of the bonding dipole peak, and the antibonding modes do not radiate significantly, and the additional damping due to absorption in the $Cu_2O$ core has a more dramatic effect. The excitons in the $Cu_2O$ core might also be expected to interact with the plasmon resonances. At room temperature, the excitons are so strongly broadened that no coupling between the excitons and the plasmons is observable in our studies.

## CONCLUSIONS

We have synthesized $Cu_2O$/Au nanoshells and examined the role of the core material in determining the optical properties of the nanoparticle. Surprisingly, the semiconducting nature of $Cu_2O$ has very little effect. The additional damping due to losses in the $Cu_2O$ core is a small contribution to the overall line width at the dipole plasmon resonance, and the excitonic line structure of $Cu_2O$ is suppressed due to thermal broadening at room temperature. Increasing the core dielectric constant increases nanoparticle absorption efficiency, reduces plasmon line width, and modifies plasmon energies. In contrast, the change in the dielectric environment significantly alters the fundamental plasmonic interactions leading to hybridized nanoshell resonances. The resulting shift in plasmon resonance wavelength results in a significant change in the optical size of the particle at the dipole resonance, leading to a change in the plasmon line width and the relative absorption and scattering cross-sections. Modifying the core medium therefore provides an additional means of tailoring both the near- and far-field optical properties in this unique nanoparticle system.

## EXPERIMENTAL SECTION

**$Cu_2O$ Nanoparticle Synthesis.** All materials were purchased from Sigma Aldrich and used without further purification. The $Cu_2O$ nanoparticles were synthesized by adapting and modifying a protocol previously reported.[43] Briefly, 4 mL of 0.01 M aqueous $CuSO_4$ solution were mixed with 16 mL of PEG dithiol (MW 1530) at various concentrations under vigorous stirring at room temperature. Subsequently, 13 mL of 0.115 M NaOH and 10.5 mL of 0.005 M ascorbic acid were mixed together in a separate vessel and quickly added to the $CuSO_4$−PEG dithiol solution mixture. The reaction was proceeded for an additional 2 min under vigorous stirring following which it was quenched by blowing an inert gas ($N_2$ or Ar) into the reaction mixture for 20 min. Depending on the particle size, the solution turns from colorless to bright yellow or orange (for smaller or larger $Cu_2O$ nanoparticles, respectively) in color. The nanoparticles were purified, and excess PEG dithiol was removed by centrifuging the nanoparticles between 5500−7000 rpm depending on particle size. All the reaction conditions are provided in Supporting Information, Table S1.

**$Cu_2O$/Au Nanoshells Synthesis.** The $Cu_2O$/Au nanoshells were fabricated by seed-mediated electroless plating of Au onto $Cu_2O$ nanoparticles. Briefly, monodisperse $Cu_2O$ nanoparticles were decorated with small gold colloid (2−3 nm) prepared by the method reported by Duff *et al.*[58] A continuous gold shell was grown around the $Cu_2O$ nanoparticles by reducing gold from an $Au^+$ plating solution onto the attached small colloid in the presence of $CO_{(g)}$.[29,30] The plating solution was prepared by mixing 50 mg of $K_2CO_3$ with 200 mL of $H_2O$ and 3 mL of a 1% $HAuCl_4$ solution and allowed to age for 24 h before using. The fabricated $Cu_2O$/Au nanoshells were centrifuged several times and finally redispersed in aqueous media to form desired particle concentrations.

**Characterization.** The nanoparticles were characterized by obtaining SEM images using a FEI Quanta 400 field emission SEM at an acceleration voltage of 25 kV, XRD patterns by using a Rigaku Ultima II vertical θ−θ powder diffractometer (Cu Kα, λ = 1.5418 Å), and absorption measurements using a Varian Cary 5000 UV−vis-NIR spectrophotometer.

*Acknowledgment.* We gratefully acknowledge the Department of Defense National Security Science and Engineering Faculty Fellowship (N.J.H.) *via* grant N00244-09-0067, the Air Force Office of Scientific Research (F49620-03-C-0068), Robert A. Welch Foundation (C1220 and C1222), and the Center for Advanced Solar Photophysics, an Energy Frontier Research Center funded by the United States Department of Energy, Office of Science, Office of Basic Energy Sciences, for financial support.

*Supporting Information Available:* XRD patterns of $Cu_2O$ nanoparticles; SEM images of $Cu_2O$ nanoparticle arrays; SEM images of $Cu_2O$/Au precursor particles; TEM images of $Cu_2O$/Au nanoshells; dielectric function of $Cu_2O$; table representing experimental parameters; calculated optical spectra of $Cu_2O$/Au nanoshells with constant real permittivity; separation of absorption in the core and shell of $Cu_2O$/Au nanoshells. Theoretical comparison of extinction spectra of $Cu_2O$/Au nanoshells with cubic cores. This material is available free of charge *via* the Internet at http://pubs.acs.org.

## REFERENCES AND NOTES

1. Brongersma, M. L. Nanoscale Photonics: Nanoshells: Gifts in a Gold Wrapper. *Nat. Mater.* **2003**, *2*, 296–297.
2. Tam, F.; Moran, C.; Halas, N. Geometrical Parameters Controlling Sensitivity of Nanoshell Plasmon Resonances to Changes in Dielectric Environment. *J. Phys. Chem. B* **2004**, *108*, 17290–17294.
3. Knight, M. W.; Halas, N. J. Nanoshells to nanoeggs to Nanocups: symmetry breaking beyond the quasistatic limit in complex plasmonic nanoparticles. *New J. Phys.* **2008**, *10*, 105006.

4. Le, F.; Lwin, N. Z.; Halas, N. J.; Nordlander, P. Plasmonic Interactions Between a Metallic Nanoshell and a Thin Metallic Film. *Phys. Rev. B: Condens. Matter Mater. Phys.* **2007**, *76*, 165410.
5. Graf, C.; Blaaderen, A. v., Metallodielectric Colloidal Core-Shell Particles for Photonic Applications. *Langmuir* **2002**, *18*, 524–534.
6. Lal, S.; Link, S.; Halas, N. J. Nano-optics from Sensing to Waveguiding. *Nat. Photonics* **2007**, *1*, 641–648.
7. Mejac, I.; Bryan, W. W.; Lee, T. R.; Tran, C. D. Visualizing the Size, Shape, Morphology, and Localized Surface Plasmon Resonance of Individual Gold Nanoshells by Near-Infrared Multispectral Imaging Microscopy. *Anal. Chem.* **2009**, *81*, 6687–6694.
8. Raschke, G.; Brogl, S.; Susha, A. S.; Rogach, A. L.; Klar, T. A.; Feldmann, J.; Fieres, B.; Petkov, N.; Bein, T.; Nichtl, A.; Kürzinger, K. Gold Nanoshells Improve Single Nanoparticle Molecular Sensors. *Nano Lett.* **2004**, *4*, 1853–1857.
9. Levin, C. S.; Kundu, J.; Barhoumi, A.; Halas, N. J. Nanoshell-based Substrates for Surface Enhanced Spectroscopic Detection of Biomolecules. *Analyst* **2009**, *134*, 1745–1750.
10. Zhao, K.; Xu, H.; Gu, B. One-Dimensional Arrays of Nanoshell Dimers for Single Molecule Spectroscopy via Surface-Enhanced Raman Scattering. *J. Chem. Phys.* **2006**, *125*, 081102.
11. Beier, H. T.; Cowan, C. B.; Chou, I.-H.; Pallikal, J.; Henry, J. E.; Benford, M. E.; Jackson, J. B.; Good, T. A.; Coté, G. L. Application of Surface-Enhanced Raman Spectroscopy for Detection of Beta Amyloid Using Nanoshells. *Plasmonics* **2007**, *2*, 55–64.
12. Huang, Y.; Swarup, V. P.; Bishnoi, S. W. Rapid Raman Imaging of Stable, Functionalized Nanoshells in Mammalian Cell Cultures. *Nano Lett.* **2009**, *9*, 2914–2920.
13. Bardhan, R.; Chen, W.; Perez-Torres, C.; Bartels, M.; Huschka, R. M.; Zhao, L. L.; Morosan, E.; Pautler, R. G.; Joshi, A.; Halas, N. J. Nanoshells with Targeted Simultaneous Enhancement of Magnetic and Optical Imaging and Photothermal Therapeutic Response. *Adv. Func. Mater.* **2009**, *19*, 3901–3909.
14. Lal, S.; Clare, S. E.; Halas, N. J. Nanoshell-Enabled Photothermal Cancer Therapy: Impending Clinical Impact. *Acc. Chem. Res.* **2008**, *41*, 1842–1851.
15. Zhou, C.; Tsai, T.-H.; Adler, D. C.; Lee, H.-C.; Cohen, D. W.; Mondelblatt, A.; Wang, Y.; Connolly, J. L.; Fujimoto, J. G. Photothermal Optical Coherence Tomography in Ex Vivo Human Breast Tissues Using Gold Nanoshells. *Opt. Lett.* **2010**, *35*, 700–702.
16. Kim, J.; Park, S.; Lee, J. E.; Jin, S. M.; Lee, J. H.; Lee, I. S.; Yang, I.; Kim, J. S.; Kim, S. K.; Cho, M.-H.; Hyeon, T. Designed Fabrication of Multifunctional Magnetic Gold Nanoshells and Their Application to Magnetic Resonance Imaging and Photothermal Therapy. *Angew. Chem., Int. Ed.* **2006**, *45*, 7754–7758.
17. Wang, Y.; Xie, X.; Wang, X.; Ku, G.; Gill, K. L.; O'Neal, D. P.; Stoica, G.; Wang, L. V. Photoacoustic Tomography of a Nanoshell Contrast Agent in the in Vivo Rat Brain. *Nano Lett.* **2004**, *4*, 1689–1692.
18. Tam, F.; Chen, A. L.; Kundu, J.; Wang, H.; Halas, N. J. Mesoscopic Nanoshells: Geometry-Dependent Plasmon Resonances Beyond the Quasistatic Limit. *J. Chem. Phys.* **2007**, *127*, 204703.
19. Knight, M. W.; Wu, Y.; Lassiter, J. B.; Nordlander, P.; Halas, N. J. Substrates Matter: Influence of an Adjacent Dielectric on an Individual Plasmonic Nanoparticle. *Nano Lett.* **2009**, *9*, 2188–2192.
20. Oubre, C.; Nordlander, P. Optical Properties of Metallodielectric Nanostructures Calculated Using the Finite Difference Time Domain Method. *J. Phys. Chem. B* **2004**, *108*, 17740–17747.
21. Wu, Y. P.; Nordlander, P. Finite-Difference Time-Domain Modeling of the Optical Properties of Nanoparticles near Dielectric Substrates. *J. Phys. Chem. C* **2010**, *114*, 7302–7307.
22. Slocik, J. M.; Tam, F.; Halas, N. J.; Naik, R. R. Peptide-Assembled Optically Responsive Nanoparticle Complexes. *Nano Lett.* **2007**, *7*, 1054–1058.
23. Fofang, N. T.; Park, T.-H.; Neumann, O.; Mirin, N. A.; Nordlander, P.; Halas, N. J. Plexcitonic Nanoparticles: Plasmon-Exciton Coupling in Nanoshell-J-Aggregate Complexes. *Nano Lett.* **2008**, *8*, 3481–3487.
24. Bardhan, R.; Grady, N. K.; Cole, J.; Joshi, A.; Halas, N. J. Fluorescence Enhancement by Au nanostructures: Nanoshells and Nanorods. *ACS Nano* **2009**, *3*, 744–752.
25. Khurgin, J. B.; Sun, G. Enhancement of Optical Properties of Nanoscaled Objects by Metal Nanoparticles. *J. Opt. Soc. Am. B* **2009**, *26*, B83–B95.
26. Averitt, R. D.; Westcott, S. L.; Halas, N. J. The Linear Optical Properties of Gold Nanoshells. *J. Opt. Soc. Am. B* **1999**, *16*, 1824–1832.
27. Brandl, D. W.; Nordlander, P. Plasmon Modes of Curvilinear Metallic Core/Shell Particles. *J. Chem. Phys.* **2007**, *126*, 144708.
28. Bardhan, R.; Mukherjee, S.; Mirin, N.; Levit, S. D.; Nordlander, P.; Halas, N. J. Nanosphere-in-a-Nanoshell: A Simple Nanomatryushka. *J Phys. Chem. C* **2010**, *114*, 7378–7383.
29. Brinson, B. E.; Lassiter, J. B.; Levin, C. S.; Bardhan, R.; Mirin, N.; Halas, N. J. Nanoshells Made Easy: Improving Au Layer Growth on Nanoparticle Surfaces. *Langmuir* **2008**, *24*, 14166–14177.
30. Oldenburg, S. J.; Averitt, R. D.; Westcott, S. L.; Halas, N. J. Nanoengineering of Optical Resonances. *Chem. Phys. Lett.* **1998**, *288*, 243–247.
31. Levin, C. S.; Hofmann, C.; Ali, T. A.; Kelly, A. T.; Morosan, E.; Nordlander, P.; Whitmire, K. H.; Halas, N. J. Magnetic-Plasmonic Core-Shell Nanoparticles. *ACS Nano* **2009**, *3*, 1379–1388.
32. Jolk, A.; Klingshirn, C. F. Linear and Nonlinear Excitonic Absorption and Photoluminescence Spectra in $Cu_2O$: Line Shape Analysis and Exciton Drift. *Phys. Status Solidi B* **1998**, *206*, 841−850.
33. Matsumoto, H.; Saito, K.; Hasuo, M.; Kono, S.; Nagasawa, N. Revived Interest on Yellow-exciton Series in $Cu_2O$: An Experimental Aspect. *Solid State Commun.* **1996**, *97*, 125–129.
34. Naka, N.; Nagasawa, N. Experimental Study on Two-photon Oscillator Strength of Hydrogenic Yellow Excitons in $Cu_2O$. *Solid State Commun.* **2000**, *116*, 417–419.
35. Karpinska, K.; Loosdrecht, P. H. M. v.; Handayani, I. P.; Revcolevschi, A. Para-excitons in $Cu_2O$ - A New Approach. *J. Lumin.* **2005**, *112*, 17–20.
36. Karpinska, K.; Mostovoy, M.; Vegte, M. A. v. d.; Revcolevschi, A.; Loosdrecht, P. H. M. v. Decay and Coherence of Two-photon Excited Yellow Orthoexcitons in $Cu_2O$. *Phys. Rev. B: Condens. Matter Mater. Phys.* **2005**, *72*, 155201.
37. Snoke, D. Spontaneous Bose Coherence of Excitons and Polaritons. *Science* **2002**, *298*, 1368–1372.
38. Hogersthal, G. B. H. v.; Dasbach, G.; Frohlich, D.; Kulka, M.; Stolz, H.; Bayer, M. Dynamic Band Gap Shifts and Magneto-Absorption of $Cu_2O$. *J. Lumin.* **2005**, *112*, 25–29.
39. Fishman, D.; Faugeras, C.; Potemski, M.; Revcolevschi, A.; Loosdrecht, P. H. M. v. Magneto-optical Readout of Dark Exciton Distribution in Cuprous Oxide. *Phys. Rev. B: Condens. Matter Mater. Phys.* **2009**, *80*, 045208.
40. Ettema, A. R. H. F.; Versluis, J. Dipole-allowed Generation of the Yellow-series Excitons in $Cu_2O$ Due to an Applied Electric Field. *Phys. Rev. B: Condens. Matter Mater. Phys.* **2003**, *68*, 235101.
41. Fröhlich, D.; Nöthe, A.; Reimann, K. Observation of The Resonant Optical Stark Effect in a Semiconductor. *Phys. Rev. Lett.* **1985**, *55*, 1335–1337.
42. Mani, S. E.; Jang, J. I.; Ketterson, J. B. Large Third-order Susceptibility and Third-harmonic Generation in Centrosymmetric $Cu_2O$ Crystal. *Opt. Lett.* **2009**, *34*, 2817–2819.

43. Gou, L.; Murphy, C. J. Controlling the Size of $Cu_2O$ Nanocubes From 200 to 25 nm. *J. Mater. Chem.* **2004**, *14*, 735–738.
44. Ribeiro, C.; Lee, E. J. H.; Longo, E.; Leite, E. R. Oriented Attachment Mechanism in Anisotropic Nanocrystals: A "Polymerization" Approach. *ChemPhysChem* **2006**, *7*, 664–670.
45. Kuo, C.-H.; Chen, C.-H.; Huang, M. H. Seed-Mediated Synthesis of Monodispersed $Cu_2O$ Nanocubes with Five Different Size Ranges from 40 to 420 nm. *Adv. Funct. Mater.* **2007**, *17*, 3773–3780.
46. Ribbing, C. G.; Roos, A. Copper Oxides ($Cu_2O$, CuO). In *Handbook of Optical Constants of Solids*; Palik, E. D., Ed.; Academic Press: San Diego, 1991; Vol. *2*, pp 875−882.
47. Barabanenkov, Y. N.; Barabanenkov, M. Y. Mie Ronances and Bragg-like Mltiple Sattering in Oacity of Two-Dimensional Photonic Crystals. *J. Opt. Soc. Am. A* **2006**, *23*, 581–585.
48. Bohren, C. F.; Huffman, D. R. *Absorption and Scattering of Light by Small Particles*; Wiley: NY, 1983; p 136−140.
49. Karlsson, B.; Ribbing, C. G.; Roos, A.; Valkonen, E.; Karlsson, T. Optical Properties of Some Metal Oxides in Solar Absorbers. *Phys. Scr.* **1982**, *25*, 826–831.
50. Zhang, J.; Liu, J.; Peng, Q.; Wang, X.; Li, Y. Nearly Monodisperse $Cu_2O$ and CuO Nanospheres: Preparation and Applications for Sensitive Gas Sensors. *Chem. Mater.* **2006**, *18*, 867–871.
51. Johnson, P. B.; Christy, R. W. Optical Constants of The Noble Metals. *Phys. Rev. B: Condens. Matter Mater. Phys.* **1972**, *6*, 4370–4379.
52. Averitt, R. D.; Westcott, S. L.; Halas, N. J. The Ultrafast Optical Properties of Gold Nanoshells. *J. Opt. Soc. Am.* **1999**, *16*, 1814–1824.
53. Wang, H.; Wu, Y.; Lassiter, B.; Nehl, C. L.; Hafner, J. H.; Nordlander, P.; Halas, N. J. Symmetry breaking in individual plasmonic nanoparticles. *Proc. Natl. Acad. Sci. U.S.A.* **2006**, *103*, 10856–10860.
54. Prodan, E.; Radloff, C.; Halas, N. J.; Nordlander, P. A Hybridization Model for the Plasmon Response of Complex Nanostructures. *Science* **2003**, *302*, 419–422.
55. Park, T.-H.; Nordlander, P. On The Nature of The Bonding And Antibonding Metallic Film and Nanoshell Plasmons. *Chem. Phys. Lett.* **2009**, *472*, 228–231.
56. Prodan, E.; Nordlander, P. Plasmon Hybridization in Spherical Nanoparticles. *J. Chem. Phys.* **2004**, *120*, 5444–5454.
57. Maier, S. A. Plasmonic field enhancement and SERS in the effective mode volume picture. *Opt. Express* **2006**, *14*, 1957–1964.
58. Duff, D. G.; Baiker, A.; Edwards, P. P. A New Hydrosol of Gold Clusters. 1. Formation and Particle Size Variation. *Langmuir* **1993**, *9*, 2301–2309.